Korean J. Chem. Eng., 38(9), 1913-1922 (2021)
DOI: 10.1007/s11814-021-0843-z

pISSN: 0256-1115
eISSN: 1975-7220

Preparation of N-TiO_2/RGO nanocomposites through sol-gel method

Yudi Ma, Shukun Wang, Wanlan Zheng, Xin Xue, Huie Liu†, Shuang Chen, and Yiwen Zhu

College of Chemical Engineering, China University of Petroleum Huadong, Qingdao 266580, Shandong Prov., China
(*Received 9 October 2020 • Revised 22 April 2021 • Accepted 12 May 2021*)

Abstract−Nitrogen-doped TiO_2 and reduced graphene oxide (RGO) nanocomposites (NTG) were prepared by sol-gel method followed by annealing treatment process under N_2 atmosphere. The as-prepared NTG nanocomposite were characterized by transmission electron microscopy (TEM), X-ray diffraction (XRD), X-ray photoelectron spectroscopy (XPS), Fourier-transform infrared spectroscopy (FT-IR) and ultraviolet-visible diffuse reflectance spectroscopy (DRS). The results indicate that the incorporation of nitrogen onto both RGO and TiO_2 was accomplished simultaneously in the facile process. Nitrogen doping makes the light excitation range red shift and can enhance the electron-hole separation effectively. The photocatalytic activity of the as-prepared samples was evaluated through the degradation of methyl orange (MO) under visible light irradiation. The introduction of nitrogen increased the photodegradation activity, which can be indicated by the fitted apparent first-order kinetics rate constant k, increasing about four times from 0-NTG-450 to 15-NTG-450. The annealing treatment further increased the photodegradation activity about 1.5 times of 15NTG-450 for 15NTG-800.

Keywords: Nitrogen-doped TiO_2, Reduced Graphene Oxide, Sol-gel Method, Methyl Orange, Visible Light Irradiation

INTRODUCTION

Environmental pollution has become a worldwide issue. Semiconductor photocatalysis is an effective way for organic pollutant degradation, hydrogen production and antibacterial actions [1]. TiO_2 is a widely studied and very important photocatalyst resulting from its optoelectronic performance, strong oxidizing ability, chemical stability, environmentally friendly property, high efficiency and low cost in removal of pollutants in air and water [2,3]. However, the great limitation of this material is its relatively high band gap (3.2 eV for anatase phase and 3.0 eV for rutile phase), allowing it to be activated mostly by UV radiation, which can only harvest 2-5% of the energy in the solar spectrum [4,5]. Under UV irradiation, electrons are stimulated from the valence band (VB) to the conduction band (CB) of TiO_2 to form electron hole pairs, which is useful for photocatalytic activity. Unfortunately, the photogenerated electrons and holes are easily recombined before they transfer to the photocatalyst surface, leading to the fast decrease of the photocatalytic efficiency for TiO_2 and limiting its applications under solar atmosphere [3,6]. Therefore, it is of great significance to extend the light response of TiO_2 from the ultraviolet range to the visible light range and inhibit the recombination of photogenerated carriers to improve the photocatalytic activity of TiO_2.

To improve the utilization of solar source, TiO_2 doped with metal/non-metal elements (C, N, S, P, Au, Pt, etc.) [7-12] and coupling with semiconductors, noble metals, polymers and carbon-based materials such as carbon black [13], CNTs [14], and graphene [15, 16] excited the interest of scientists. That said, in the process of transition metal catalysis, the leaching of toxic metals often occurs, causing potential harm to human health, which limits its practical application in environmental pollution control [17,18]. Among the different kinds of substances mentioned, nitrogen as a dopant has attracted much attention resulting from its efficiency in the preparation of visible light-responsive photocatalysts [19-21]. Combination of TiO_2 and nanostructured carbon materials (encompassing zero-dimensional, one-dimensional, or two-dimensional materials) provides a wide range of potential applications [22-24].

As a single-layer six-membered ring composed of sp2 hybrid carbon atoms, graphene has attracted attention greatly since its discovery [25]. Due to its unique properties, graphene has high carrier mobility (>200,000 $cm^2\ V^{-1}\ s^{-1}$), good thermal conductivity (5,000 $W\ m^{-1}\ K^{-1}$) and extremely high theoretical specific surface area (2,600 $m^2\ g^{-1}$) [26]. So the combination of TiO_2 and graphene is an attractive way for improving the property of TiO_2.

Graphene oxide (GO) is always used in the preparation of TiO_2/graphene composite materials because the non-easily dispersible property of graphene in water. However, the electrical conductivity of GO is much lower than graphene because the highly conjugated structure of graphene is destroyed by oxygen-containing functional groups. By reducing graphene oxide (GO), most of the oxygen-containing functional groups, such as epoxide [27], can be removed to form reduced graphene oxide (RGO). Meanwhile, due to the partial reconstruction of the conjugated structure in the reduction process, the conductivity of GO is significantly improved. The results show that RGO can be used as an ideal electron trap or electron transfer bridge. When combined, RGO can slow down the charge recombination, accelerate the electron transfer and improve the photocatalytic efficiency of TiO_2 [28-32].

Among the above-mentioned candidates, nitrogen and RGO have gained widespread concern, resulting from their efficiency in preparing visible light-responsive photocatalysts. Mohammadi et al. [33] prepared RGO-TiO_2 nanocomposites by means of hydrother-

†To whom correspondence should be addressed.
E-mail: liuhuie@upc.edu.cn

mal approach using TiO_2 powder and GO nanosheets, which degraded 90% of 20 ppm methylene blue in 15 min. Pei et al. [34] fabricated a reduced graphene oxide (TRG-COOH) nanocomposite photocatalyst by mixing TiO_2 with RGO, and its photocatalytic efficiency was about 8.9 and 2.7 times that of P25 and fully reduced TiO_2-RGO composite under Xenon lamp. Ida et al. [35] reported a photocatalyst through simultaneous doping of nitrogen (using 10% ammonia solution as nitrogen precursor) and RGO on TiO_2 under ultrasonic conditions followed by hydrothermal method. It can promote the production of H_2, reaching 15,028 μmol/h/g under UV-Vis irradiation.

The existing modification method of TiO_2 mostly is based on solvothermal method, but there are several limitations such as high pressure and temperature, long reaction time and so on. To solve these problems, the sol-gel method attracted attention because it is mild for obtaining TiO_2 nanocomposite. The time-consuming step (long-time reaction) is eliminated in the synthesis process without interrupting the conformation process of TiO_2 nanoparticles, which is essential for obtaining crystalline TiO_2 [36]. There are reports on N doping of GO [37,38] or TiO_2 [16,22], but there are few reports about nitrogen doping on TiO_2/RGO nanocomposites. Especially, as far as we know, the nitrogen doping of TiO_2 and RGO has not been studied for sol-gel synthesis. Furthermore, the role of the N dopant on organic pollutant degradation needs to be further clarified. Simultaneously, a plausible mechanism should be established to prove how the nitrogen source, RGO and TiO_2 simultaneously take effect in a photocatalytic reaction.

Simultaneous doping of nitrogen through sol-gel method using urea as nitrogen source on both TiO_2 and RGO was to be carried out. The prepared photocatalyst was accessed for dye degradation. The suitable preparation conditions and N doping amount which are favorable for dye degradation are to be discussed. Successful introduction of nitrogen simultaneously onto TiO_2 and RGO was confirmed by various characterization methods, and possible reaction mechanism of the degradation process was analyzed.

EXPERIMENTAL

1. Materials

Tetrabutyl titanate ($C_{16}H_{36}O_4Ti$, ≥99.0%), ethanol (C_2H_6O, ≥99.9%), acetylacetone ($C_5H_8O_2$, ≥99.0%), nitric acid (HNO_3, ≥99.9%), potassium permanganate ($KMnO_4$, ≥99.0%), sodium nitrate ($NaNO_3$, ≥99.0%), concentrated sulfuric acid (H_2SO_4, ≥99.9%), hydrogen peroxide (H_2O_2, ≥99.0%) and urea (CH_4N_2O, ≥99.0%) were purchased from Sinopharm Ltd. All chemical reagents were used as received without further purification. Deionized water was used in all the experiments.

2. Synthesis of Graphite Oxide

Graphite oxide was synthesized following modified Hummers' method [39]. The yellow graphite oxide suspension obtained was washed with dilute hydrochloric acid to remove impurities and then washed thoroughly with distilled water until the pH of the supernatant reached 7 [40]. At the end, the obtained graphite oxide solution was dried in vacuum at −40 °C for 24 h.

3. Synthesis of Nitrogen-doped TiO_2/Reduced Graphene Oxide

The nitrogen-doped TiO_2/reduced graphene oxide (NTG) nanoparticles were synthesized by a sol-gel method followed by an annealing treatment. Urea was selected as nitrogen dopant compound.

Tetrabutyl titanate and acetylacetone (volume ratio between these two reagent was 1 : 1, 2 ml for each) was added drop-by-drop into 40 ml ethyl alcohol under vigorous magnetic stirring for 2 h and a nanocolloid (sol-TiO_2) suspension was formed. Then 15 mg urea was dissolved into 10 ml ethyl alcohol. The urea solution was dropwise added into the sol-TiO_2 under vigorous magnetic stirring for 2 h to form nitrogen-doped gel-TiO_2. A mixture of certain amount of graphite oxide and 40 ml deionized water was treated under ultrasonic oscillation to form graphene oxide (GO) solution. The solution of GO was then dropwise added into the nitrogen-doped gel-TiO_2, with 0.5 ml mixture of nitric acid and ethyl alcohol (1 : 10 (V/V)) added together so as to avoid the destruction of the stable gel system. The mixture was stirred for 1.5 h and then dried at 80 °C. The obtained dried powders were calcined at 450, 600, 700, 800 °C, respectively, in nitrogen atmosphere for 1 h to obtain NTG photocatalysts.

The effect of urea concentration was also studied through varying the weight of urea added (0, 5, 15, 50, 100 and 500 mg). The annealing temperature was also varied (T=450, 600, 700 and 800 °C, respectively) to observe its influence on NTG photocatalysts. The prepared NTG photocatalysts were named as *x*NTG-*T* to distinguish the amount of urea added and the annealing temperature used, where x is the weight of urea added, with x=0, 5, 15, 50, 100 and 500 mg, respectively; and *T* is the annealing temperature used, with T=450, 600, 700 and 800 °C, respectively.

4. Characterization Methods

The diffuse reflectance spectra of the catalysts were studied by Shimadzu UV-2501 PC integrating sphere spectrophotometer. The crystal structure of TiO_2 nanoparticles was characterized by powder X-ray diffraction (XRD, Bruker D8 discover diffractometer) analysis using Cukα radiation (λ=1.5406 Å) at 40 kV/40 ma with an angle range of 20-60° (2θ). Rietveld refinement was used for subsequent X-ray diffraction data analysis. The Kratos Axis-Supra instrument with aluminum Kα monochromatized radiation source was used to measure X-ray photoelectron spectroscopy (XPS). At 284.8 eV, all the binding energies are at the C1s level. The surface morphology was observed by SEM (SEM, Carl Zeiss, SUPRA-55) and high resolution transmission electron microscopy (HRTEM, FEI, TECHNAI F20, Supertwin) techniques.

5. Photocatalytic Activity Analysis

The photocatalytic activity of different catalyst samples was evaluated through the photocatalytic degradation effects of methylene blue (MB, 20 mg/L, λ_{max}^{op}=664 nm) and methyl orange (MO, 20 mg/L, λ_{max}^{op}=464 nm), under visible irradiation. The visible irradiation source employed was a 500 W xenon lamp filtered to 400-800 nm range so as to avoid the disturbance of ultraviolet. 100 mg of one kind photocatalysts and 200 ml of dye aqueous solution were added to the reaction system and ultrasonic wave was conducted for 30 min in the dark to ensure adsorption-desorption equilibrium. The xenon lamp was turned on afterwards and the photodegradation process began. During the photodegradation process, 4 ml solution samples were extracted at a certain time interval, and the photocatalysts were separated from the solution samples by centrifugation. The concentration of residual transparent solu-

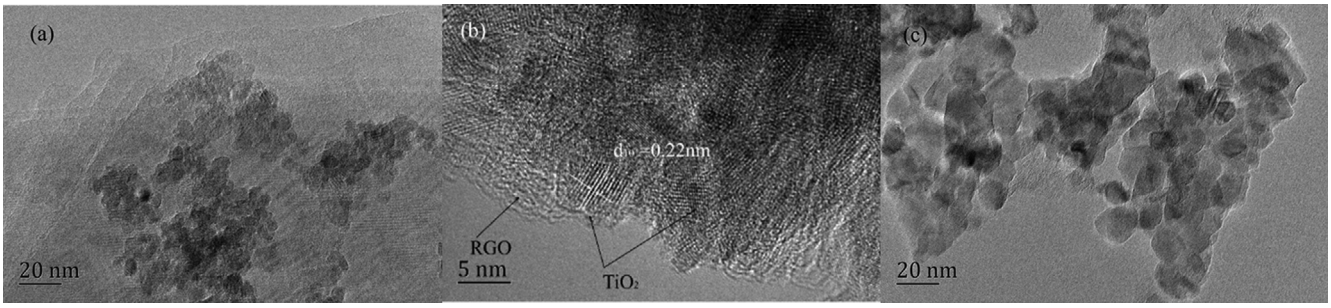

Fig. 1. TEM image of 15NTG-450 (a)-(b) and 15NTG-800 (c).

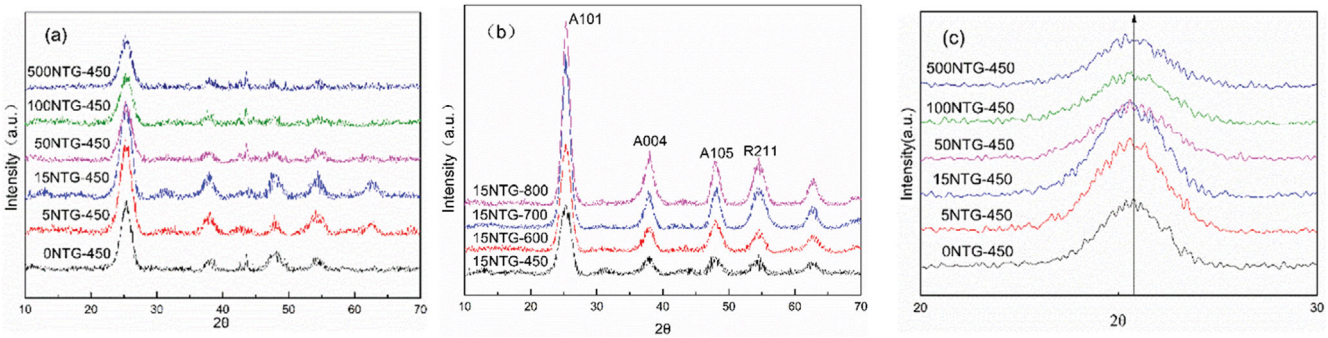

Fig. 2. (a) XRD patterns of 0NTG-450, 5NTG-450, 15NTG-450, 50NTG-450, 100-450NTG and 500NTG-450; (b) XRD patterns of 15NTG-450, 15NTG-600, 15NTG-700 and 15NTG-800; (c) details at 25.3° in (a).

tion was analyzed by UV-Visible spectrophotometer (Shanghai Jingke UV-752N).

RESULTS AND DISCUSSION

1. Morphology Analysis

As is known, the morphology of nanocomposites has a certain influence on the photocatalytic activity. Hence, the morphology of NTGs was observed by TEM. Fig. 1 gave the TEM image of 15NTG-450 (a)-(b) and 15NTG-800 (c). From the normal magnification images (Fig. 1(a)), the general diameters of TiO_2 nanoparticles were about 8-10 nm. The two-dimensional structure partially with wrinkles could be identified as the RGO sheets in the nanocomposites. From the high resolution TEM image shown in Fig. 1(b), RGO nanosheets covered the TiO_2 nanoparticles in the nanocomposites in some degree. Besides, the fringe spacing was measured to be 0.22 nm, which could be vested in the (101) crystal facet of anatase. With the increase of annealing temperature, more N-doped TiO_2 nanoparticles were anchored by RGO and RGO monolayers were not damaged by higher temperature, which can be shown in Fig. 1(c). As shown in Fig. 1(c), diameter of TiO_2 particles was a little larger compared to Fig. 1(a) when the annealing treatment temperature rose from 450 to 800 °C. Pei et al. [41] also found that the increase of annealing treatment temperature could significantly change the diameters of TiO_2 particles, with slightly larger particle size observed under higher annealing treatment temperature.

2. XRD Patterns

The crystallinity of different catalysts was analyzed by X-ray diffractometer. Fig. 2(a) and (b) show XRD plots of *x*NTG-*T* corresponding to various urea added amounts and annealing temperature. Fig. 2(c) shows the detail at the 2θ angle of 25.3° of Fig. 2(b). As shown in the XRD patterns, anatase was the major phase and rutile was the secondary phase. The diffractogram of all TiO_2 based samples has peaks at 2θ angles 25.3°, 37.8°, 48.1°, 54.2° and 55.1° that correspond to (101) (004) (105) and (211) planes. All the catalysts showed the presence of anatase phase of TiO_2 (JCPDS-No.21-1272) with prime existence of plane (101). The absence of characteristic peak of GO at 22° for *x*NTG-*T* proved that TiO_2 had a good separation effect on RGO nanosheets [42]. The obvious increasing first and then decreasing in the peak intensity at 25.3° with the increase of nitrogen doped onto the TiO_2 verified the high crystallinity after doping with proper content of nitrogen, which can be seen in Fig. 2(a). The higher the crystallinity, the higher the

Table 1. XRD data of the samples

No.	Sample	d (nm)	D (nm)
1	0NTG-450	3.4398	21.4
2	5NTG-450	3.5281	9.4
3	15NTG-450	3.5010	9.1
4	50NTG-450	3.5223	10.3
5	100NTG-450	3.5146	10.9
6	500NTG-450	3.5622	11.2
8	15NTG-600	3.4875	9.5
9	15NTG-700	3.5228	9.9
10	15NTG-800	3.5145	10.5

Note: d- interplanar spacing; D- crystallite size

energy band structure of the semiconductor, and the stronger photocatalytic activity [43,44]. Simultaneously, annealing treatment can significantly improve the degree of crystallization, especially facets (101), (004) and (105) as shown in Fig. 2(b). To measure the structural changes quantificationally, Scherrer's equation [42] was used to determine the crystallite size and Table 1 presented XRD data of the nanocomposites. As shown in Table 1, mean crystallite size decreased from 21.4 nm for sample 1 to 9.1 nm for sample 3 but increased to 11.2 nm for sample 6. The decrease of peak width leads to the increase of microcrystalline size compared with the non-N-doping sample (0NTG-450), which proved that nitrogen element was successfully induced into the TiO_2 shown in Fig. 2(a). The crystal form could behave more obviously with the increase of annealing treatment temperature confirmed by Fig. 2(b) where the peak was gradually sharpened. As shown in Table 1, diameter of TiO_2 particles was a little larger when the annealing treatment temperature rose from 450 to 800 °C, which could also be proved by TEM images in Section 3.1. The slight deviation of 2θ value of xNTG-450 (Fig. 2(c)) indicated the stress is caused by nitrogen doping in the nanocomposites.

3. XPS Spectra

The NTG samples fabricated via the N-doping under anneal-

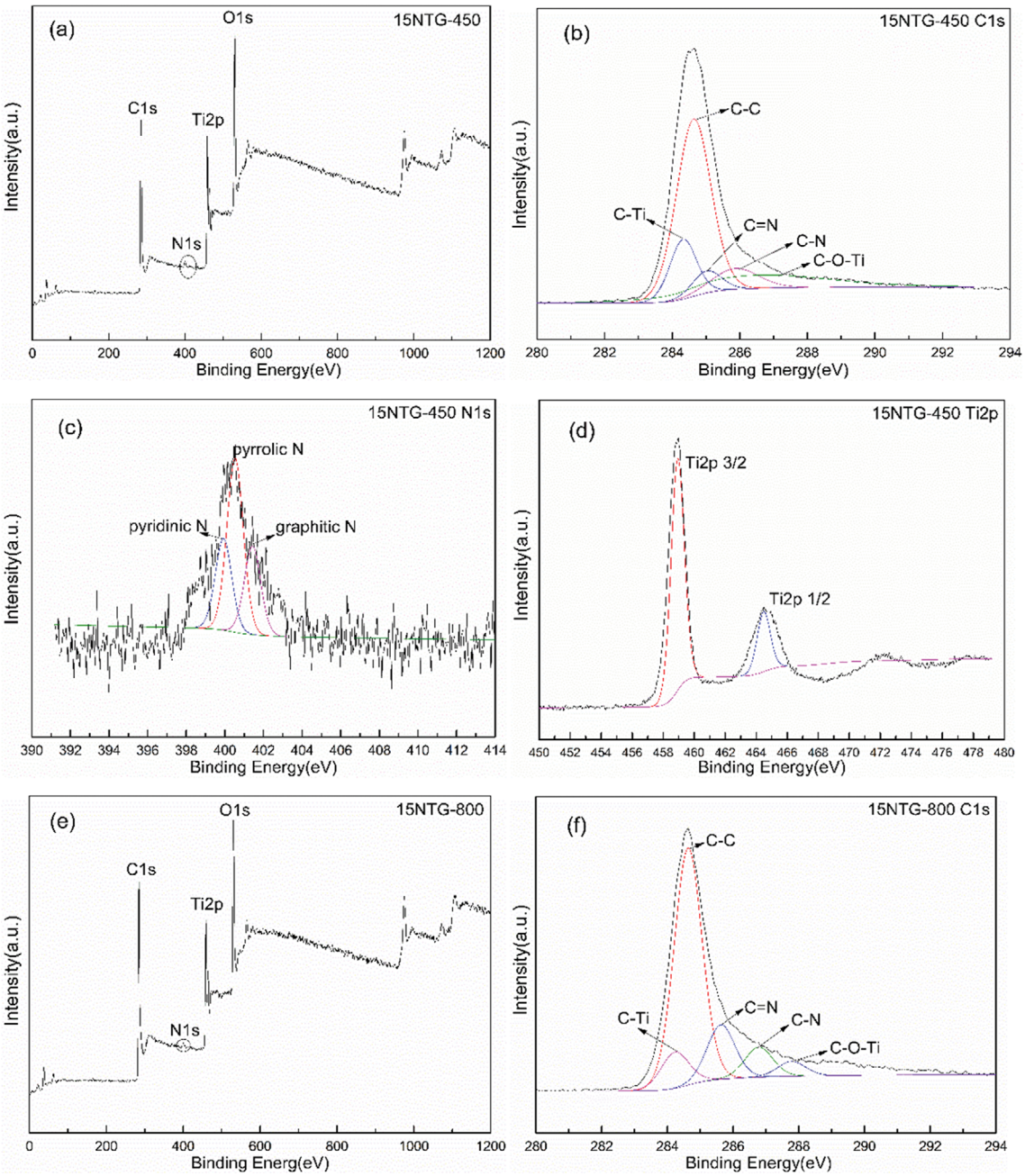

Fig. 3. XPS full-scale spectra of 15NTG-450 (a) and 15NTG-800 (e); high-resolved XPS spectra of C1s ((b) 15NTG-450 and (f) 15NTG-800); high-resolved XPS spectra of N1s ((c) 15NTG-450); high-resolved XPS spectra ofTi2p ((d) 15NTG-450).

ing treatment were analyzed by XPS spectra to prove the N-doping effect. The high-resolved XPS spectrum was fitted by Gaussian-Lorentzian sum function employing professional fitting software (Casa XPS). The XPS spectra of 15NTG-450 in Fig. 3(a) and 15NTG-800 in Fig. 3(e) revealed the signals of C1s, O1s, Ti2p and N1s with binding energies of 285 eV, 530 eV, 459 eV and 400 eV, respectively. The binding energy of 400 eV in Fig. 3(a) and (e) showed the existence of nitrogen in NTG samples, suggesting the successful N-doping of the samples. The Gaussian fitting of C1s region of sample 15NTG-450 is shown in Fig. 3(b), where the peak at 284.3 eV is identified as the nonoxygenated carbons. This is the characteristic peak of sp2 carbon (C-C) in the graphite network, representing the favorable regain of sp2 hybrid carbon after annealing. The peak at 286.0 eV demonstrates the existence of C-N, and the peak at 285.2 eV shows the feature of C=N group on RGO. The nitrogen element in the NTG sample was recognized as pyridinic N, graphitic N and pyrrolic N from the high resolution XPS analysis of N1s (Fig. 3(c)). The chemical anchoring effect produced by the existence of C-Ti and C-O-Ti after annealing treatment guaranteed the uniform distribution of TiO_2 nanoparticles on RGO nanosheets shown by the high-resolution XPS spectra of C1s (Fig. 3(b) and (f)) [45-48]. The agglomeration of TiO_2 nanoparticles and the accumulation of RGO monolayer was hindered by the above effect [49,50], which would offer more active sites for photocatalytic performance.

As shown in Table 2, atomic concentration of N1s gradually increased among samples 1 to 6. Apart from the Ti2p 1/2 peak, Ti2p 3/2 was identified as the signal of 456.2 eV. When sample 3 was compared with sample 7, it can be deduced that the phase changed slightly from anatase to rutile with the increasing of annealing temperature, as also proved by the XRD analysis in Section 3.2. For the samples annealed at 450 °C, significant characteristic peaks appeared at lower binding energies, universally analyzed as Ti^{3+}. This was the evidence for the existence of the major phase of Ti-N in NTGs [51], justifying the effective N-doping of TiO_2.

As shown in Table 2, atomic concentration of Ti2p slightly decreased when the annealing treatment temperature rose from 450 °C to 800 °C, and the increase of C1s indicated that RGO monolayer was more evenly distributed and closer binding to TiO_2 nanoparticles. By comparing Fig. 3(f) with Fig. 3(b), it can be seen the peak area of C-N and C=N obviously increased for 15NTG-800, indicating that higher annealing treatment temperature could make more nitrogen attached to RGO nano-sheets. Larger peak area of C-O-Ti confirmed that higher annealing treatment temperature could improve the combination of RGO and TiO_2.

4. FT-IR

The functional groups on the surfaces of 0NTG-450, 15NTG-450 and 15NTG-800 were investigated by FT-IR (Fig. 4). Peaks at 512 and 791 cm^{-1} result from the vibration of Ti-O-Ti and Ti-O-C bonds, respectively. Small peak at 1,207 cm^{-1} of 15NTG-450 samples corresponds to Ti-N bond, which cannot be observed in FT-IR spectra of 0NTG-450 as shown in Fig. 4(a) and reflects a little

Table 2. Atomic concentration and mass concentration characterized by XPS spectra

No.	Sample	Atomic concentration %				Mass concentration %			
		O1s	Ti2p	N1s	C1s	O1s	Ti2p	N1s	C1s
1	0NTG-450	20.86	7.50	-	71.64	21.28	23.91	-	54.81
2	5NTG-450	22.61	9.95	1.94	65.50	21.63	29.75	1.62	47.00
3	15NTG-450	24.65	11.26	2.02	62.07	22.79	32.53	1.63	43.04
4	50NTG-450	22.69	9.85	2.50	64.96	21.77	29.53	2.10	46.68
5	100NTG-450	22.19	9.02	2.61	66.18	21.72	27.59	2.23	48.52
6	500NTG-450	22.53	9.26	2.65	65.56	21.88	28.11	2.25	47.76
7	15NTG-800	21.73	9.18	1.90	67.19	21.21	28.00	1.62	49.18

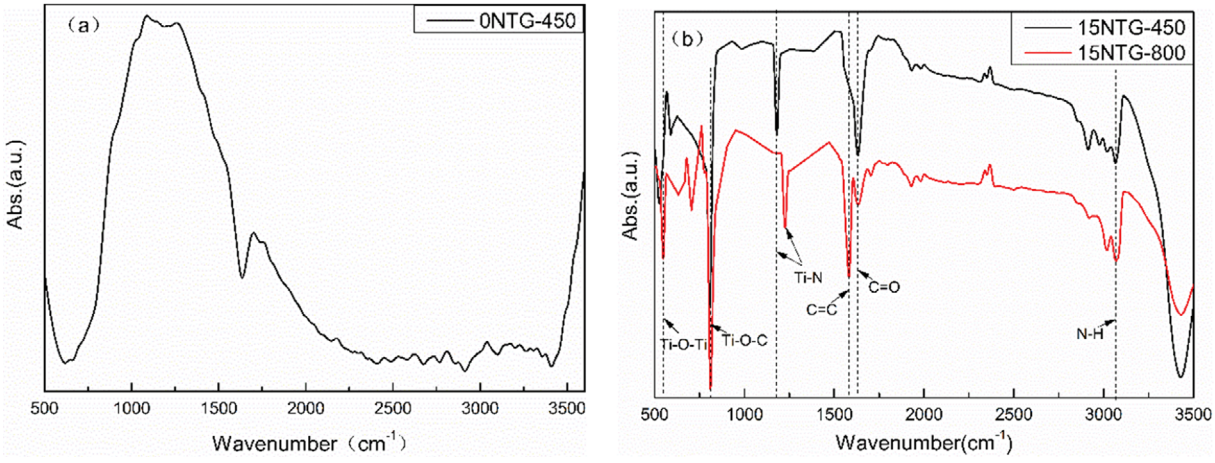

Fig. 4. FT-IR spectra of 0NTG-450 (a), 15NTG-450 and 15NTG-800 (b).

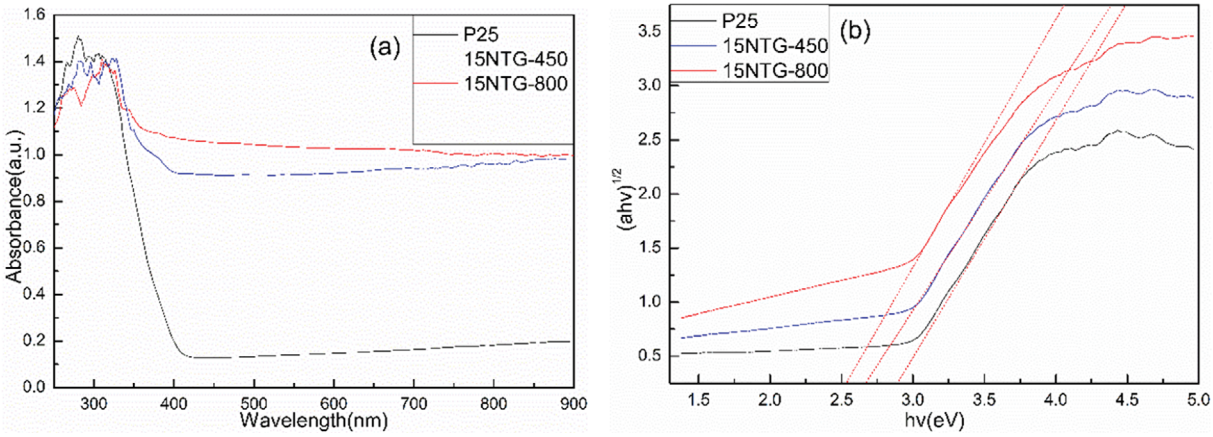

Fig. 5. UV-vis DRS spectra (a) and plots of ($\alpha h\nu$)1/2 versus photon energy ($h\nu$) of P25, 15NTG-450 and 15NTG-800 (b).

offset along with increasing of annealing treatment temperature shown as 15NTG-800 because of the introduction of nitrogen [50]. Ti-N bond was also observed in the XRD results in Section 3.3. The peaks of C=C and C=O on RGO surface appear at 1,630 cm^{-1} and 1,700 cm^{-1} separately (Fig. 4(b)). The 15NTG-450 and 15NTG-800 samples show individual peaks of N-H group on the pyrrole ring at 3,100 cm^{-1}. These signals appeared after nitrogen doping, implying that the oxygen-containing groups were reduced, which could result in the π-π reconstruction of π-conjugated system, helping to improve the separation and transport of carriers and reduce the recombination probability of the photogenic carrier. Thus, the presence of N-H group confirms the mechanism participation with the stable existent of pyrrolic nitrogen.

5. UV-vis DRS

The method of ultraviolet-visible (UV-vis) DRS was applied for estimating the band gap of nanocomposites. The UV-vis DRS of pristine TiO_2 (P25), 15NTG-450 and 15NTG-800 were exhibited (Fig. 5). The reflectivity data was calculated on the basis of relative reflectivity percentage to $BaSO_4$. The P25 only responds to ultraviolet light and performs an absorption limit at wavelength of 400 nm. Compared to P25, the spectra of NTG samples show a red shift of the absorption edge shown in Fig. 5(a). This allows NTG nanocomposites to show better photocatalytic efficiency than pure TiO_2 (P25), resulting from the presence of visible light motivated photogenerated carriers [52]. A link between ($\alpha h\nu$)1/2 and photon energy ($h\nu$) is shown (Fig. 5(b)). The band gaps reckoned from the transformation diagram of Kubelka-Munk function are 2.91 eV of P25, 2.67 eV of 15NTG-450 and 2.54 eV of 15NTG-800. The band gap is narrowed, hence the energy required for photoactivation is reduced [53], which can be attributed to the N-doping and the composition of RGO.

6. Photoluminescence Analysis

Photoluminescence (PL) analysis was used to detect electronic energy transfer between RGO and TiO_2. Because the photoluminescence emission comes from the recombination of excited electrons and holes under light irradiation, the higher photoluminescence intensity shows the separation and combination of more photo-induced electrons and holes inside the materials. The PL spectra of P25, 15NTG-450 and 15NTG-800 are shown in Fig. 6.

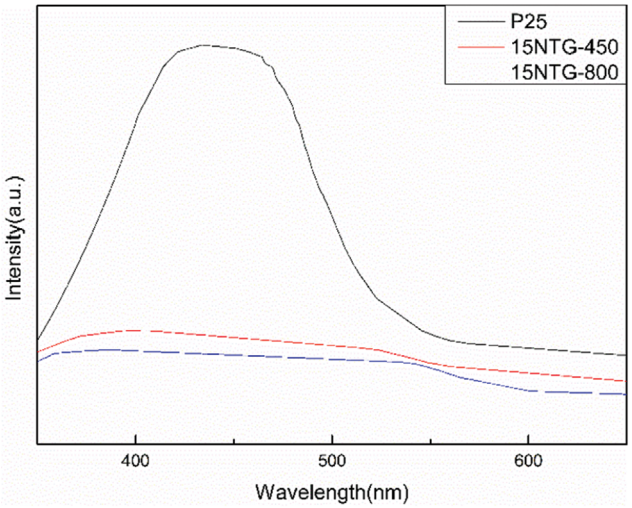

Fig. 6. Photoluminescence spectra of P25, 15NTG-450 and 15NTG-800.

P25 gave a broad emission peak between 400 and 550 nm. However, the emission peak of 15NTG-450 and 15NTG-800 was quenched significantly, meaning that anti-recombination of photoelectrons and holes had occurred. As electron-transporting bridge and electron sink, RGO can help avoid the bulk/surface charge recombination by efficient charge separation and fast charge transportation. This is necessary for the enhancing of photocatalysis.

7. Photocatalytic Assessment

The photodegradation performance of NTG was evaluated under irradiation of Xenon lamp (500 W) with ultraviolet light (<400 nm) to be cut by a UVCUT420 optical filter. MO was used as a photodegradable substrate. Dye degradation rate was defined as the amount of degraded dye divide by that of the original dye after certain time to quantitatively measure the photocatalytic activity, as shown in Eq. (1).

$$D=1-C/C_i \quad (1)$$

where D is dye degradation rate at time t, C_i nd C are the initial concentration of MO and that at time t. Fig. 7 gives the photodeg-

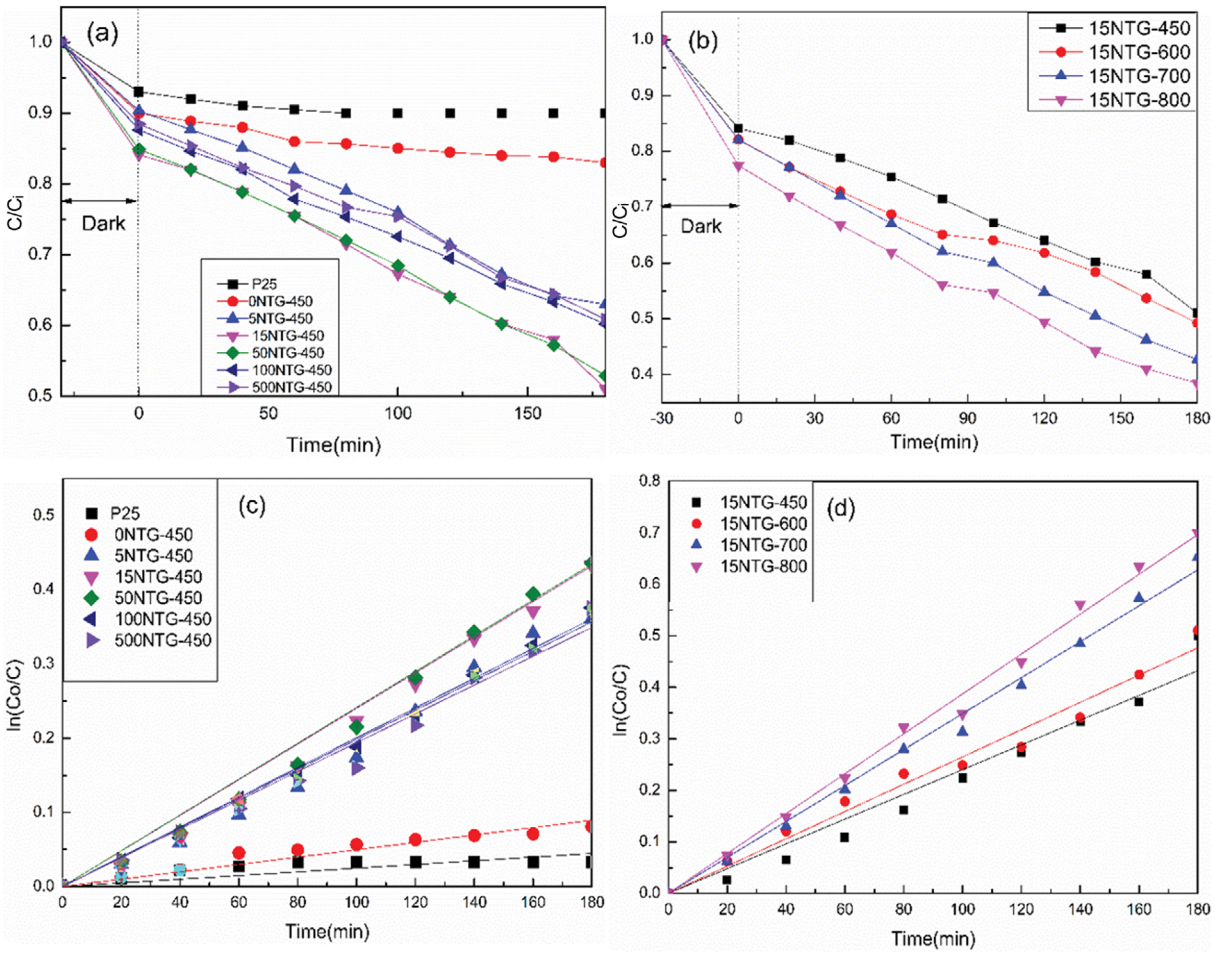

Fig. 7. Photodegradation performance of nanocomposites *x*NTG-450 (a) and 15NTG-*T* (b); relationship between irradiation time and ln(C_o/C) deduced from the photodegradation data of *x*NTG-450 and 15NTG-*T* shown in (c) and (d).

radation performance of nanocomposites *x*NTG-450. Fig. 7(a) suggests that the degradation rate of methyl orange was only 17.00% in 210 min for 0NTG-450 nanoparticles under visible light irradiation. While for 15NTG-450, the MO dye degradation rate was 49.00% in 210 min as illustrated in Fig. 6(a).

First-order kinetics fitting was often used in previous studies, and it also shows good fitting effect for first-order kinetics in this work (Table 3). C_0 and C are the concentration of MO after dark adsorption and that at time t. The kinetics of the photodegradation reaction can be illustrated using a first-order kinetics, see Eq. (2).

$$\ln(C_0/C)=kt \quad (2)$$

where C_0 and C are the same as Eq. (1), and k is the apparent first-order kinetics rate constant. Fig. 7(c) and (d) show the linear relationship between ln(C_0/C) vs. the reaction time for the corresponding photocatalysts. The fitting results are summarized in Table 3, including dye degradation rate, D after 180 min illumination under visible light and corresponding apparent first-order kinetic rate constants. The introduction of nitrogen in NTG led to the improvement of photodegradation efficiency. The rate constant k to about 4.8 times for 15NTG-450 (which was considered as the most efficient photocatalyst) when compared with 0NTG-450. The presence of nitrogen in the NTGs was confirmed in Section 3.3, which will reduce the band gap, partially reconstructing the π-conjugated structure. These changes enhance the suitable separation of photogenerated carriers and nitrogen-doped π-π reciprocity in NTG [54,55]. As the content of nitrogen increased,

Table 3. Dye degradation rate and apparent first-order kinetics rate constant k of *x*NTG-*T*

No	Sample	D, %	k, 10^{-3} min^{-1}	Determination coefficient, R^2
1	0NTG-450	17.00	0.50	0.9916
2	5NTG-450	37.02	1.98	0.9984
3	15NTG-450	48.96	2.40	0.9923
4	50NTG-450	47.10	2.42	0.9953
5	100NTG-450	39.81	2.01	0.9923
6	500NTG-450	39.16	1.94	0.9980
7	15NTG-600	50.71	2.65	0.9938
8	15NTG-700	57.28	3.49	0.9979
9	15NTG-800	61.50	3.87	0.9983

some of TiO_2 nanoparticles were wrapped by the wrinkled RGO nanosheet, which hindered their absorption of visible light [56], even decreasing the production of photogenerated carriers on TiO_2. This explanation could be well confirmed by photodegradation results shown in Fig. 7(a). As shown in Fig. 7(a), photocatalytic efficiency obviously increased from nitrogen content of 0 mg to 15 mg, but decreased from 15 mg to 500 mg.

Annealing temperature also shows important influence on photocatalytic efficiency, which obviously increased when the annealing treatment temperature increased from 450 °C to 800 °C, as shown in Fig. 7(b). The photodegradation rate constant k increased to about 1.6 times of 15NTG-450 for 15NTG-800, as shown in Fig. 7(d) and Table 3. The change of photocatalytic efficiency results from the significant change of the crystal structure of TiO_2 when the annealing treatment temperature increased from 400 to 800 °C. Changing of crystal structure can intuitively reflect in Section 3.2. As shown in Fig. 2(b) and Fig. 7(b), anatase phase is proved as the main phase of photodegradation. Obviously, N-doping can enhance sensitivity to visible light, and higher annealing treatment temperature can greatly improve photodegradation efficiency.

8. Plausible Mechanism

The plausible mechanism for the photocatalytic degradation of the organic dye is depicted in Fig. 8. Under sunlight irradiation, NTG nanocomposite photocatalyst gets activated and electron-hole are formed. The formed electrons transfer to conduction band (CB) and holes are generated in the valance band (VB). However, recombination of electron and hole is substantial. which drastically reduces the photocatalytic activity in presence of only TiO_2. Deposition of TiO_2 nanoparticles on RGO nanosheets with the aid of annealing treatment enhances the trapping of electrons to conduction band in RGO nanosheets, which substantially reduces the recombination rate of electron-hole pair. The excited electrons will be released from the surface of TiO_2 to the RGO nanosheets. Profiting from high electron mobility (>1,000 cm^2 V^{-1} s^{-1}) of RGO [57], charge separation and obstructing the electron-hole pair recombination occur rapidly. In addition, high surface area of RGO enhances the adsorption of organic dye on the formed NTG nanocomposite, which in turn improves the degradation rate of dye under sunlight.

The energy level of N2p dopant is 2.48 eV below the CB of TiO_2 [58]. Obviously, after visible light irradiation, the electrons in NTG are aroused from N2p dopant energy level to CB. NH_2• radical rapidly combines with carboxyl group on RGO surface for forming fundamental amide group. Intramolecular dehydrolysis will happen between the neighboring hydroxyl groups on RGO and amide group for forming pyrrole or pyridinic nitrogen on NTG nanocomposites where pyrrolic nitrogen plays a major reactive role [59]. The oxygen functional groups are reduced partially after annealing treatment. On the other hand, anchoring positions of TiO_2 on RGO nanosheets gives the credit to nitrogen element, which promotes light induced electron transfer between them. These free electrons related to the sp2 carbons in NTG nanocomposite can be excited by conjugation effect with electrons in pyrrolidine nitrogen, thereby enhancing the photocatalytic activity [52,60].

CONCLUSION

Nitrogen-doped reduced graphene cxide/Titanium dioxide (NTG) photocatalysts were compounded by N-doping TiO_2 and RGO through sol-gel method to observe the effect of nitrogen-doping in NTG-*x* during the photodegradation performance. Simultaneously, different nitrogen content and different annealing treatment temperature were adopted for achieving the respective effect of nitrogen-doping process of NTG-*x* nanocomposites during the photodegradation performance under visible light. XPS, FT-IR, UV-vis DRS, XRD and TEM were used to characterize the nanocomposites. The XPS signal of nitrogen element at the binding energy of

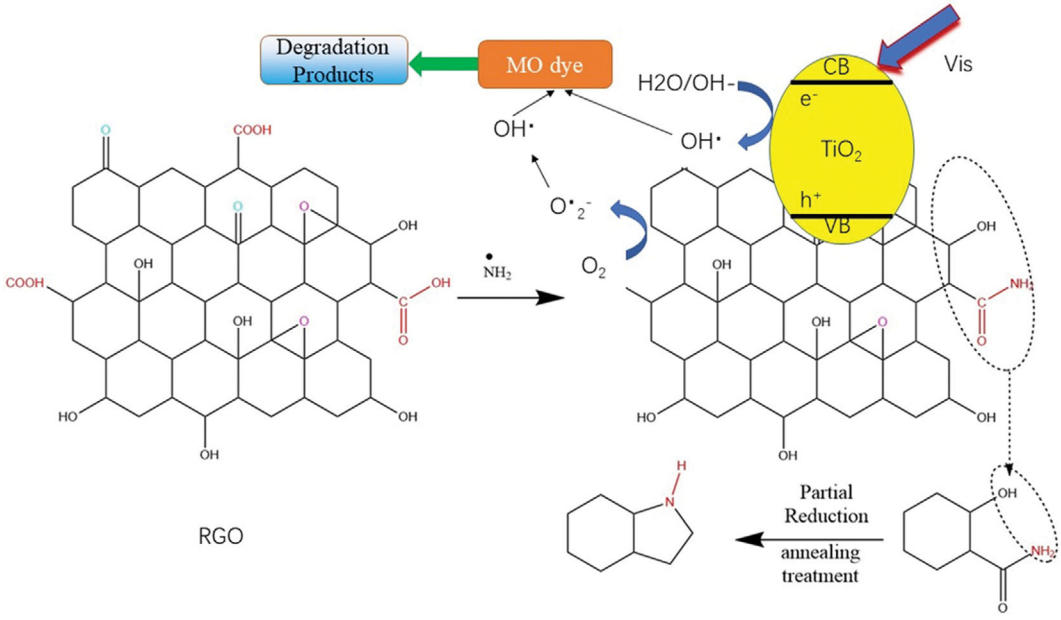

Fig. 8. Schematic diagram of possible photocatalytic mechanism for photocatalytic degradation of MO dye.

400 eV implied N-doping existing in NTG. Hence, the photodegradation ability of NTG under visible light, with methyl orange as a photodegradable object, exceeds that of 0NTG-450. The fitted apparent first-order kinetic rate constant k implied that the introduction of nitrogen element increases about 2.8 times from 0NTG-450 to 15NTG-450 of the photodegradation activity and the annealing treatment further increases about 1.6 times from 15NTG-450 to 15NTG-800.

DECLARATION OF COMPETING INTEREST

The authors declare that they have no known competing financial interests or personal relationships that could have appeared to influence the work reported in this paper.

ACKNOWLEDGEMENT

The authors thank the financial support of National Natural Science Foundation of China (22078366).

REFERENCES

1. B. Jiang, C. Tian, Q. Pan, Z. Jiang, J. Wang, W. Yan and H. Fu, *J. Phys. Chem.*, **115**, 23718 (2011).
2. W. Gao, M. Wang, C. Ran, X. Yao, H. Yang, J. Liu, D. He and J. Bai, *Nanoscale*, **6**, 5498 (2014).
3. S. G. Kumar and K. S. R. K. Rao, *Appl. Surf. Sci.*, **391**, 124 (2017).
4. G. Liu, Y. N. Zhao, C. H. Sun, F. Li, G. Q. Lu and H. M. Cheng, *Angew. Chem. Int. Ed.*, **47**, 4516 (2008).
5. M. S. A. S. R. Shah, A. R. Park, K. Zhang, J. H. Park and P. J. Yoo, *ACS Appl. Mater. Interfaces*, **4**, 3893 (2012).
6. Y. Y. Wen, H. M. Ding and Y. K. Shan, *Nanoscale*, **3**, 4411 (2011).
7. X. B. Chen, S. H. Shen and L. J. Guo, *Chem. Rev.*, **110**, 6503 (2010).
8. Y. X. Zhao, X. F. Qiu and C. Burda, *Chem. Mater.*, **20**, 2629 (2008).
9. T. Ohno, T. Mitsui and M. Matsumura, *Chem. Lett.*, **32**, 364 (2003).
10. Y. Choi, T. Umebayashi and M. Yoshikawa, *J. Mater. Sci.*, **39**, 1387 (2004).
11. H. X. Li, Z. F. Bian, J. Zhu, Y. N. Huo, H. Li and Y. F. Lu, *JACS*, **129**(15), 4538 (2007).
12. M. W. Kadia and R. M. Mohamed, *Ceram. Int.*, **45**, 6058 (2019).
13. X. Zhou, B. Jin, L. Li, F. Peng, H. Wang, H. Yu and Y. Fang, *J. Mater. Chem.*, **22**, 17900 (2012).
14. W. Chen, Z. Fan, B. Zhang, G. Ma, K. Takanabe, X. Zhang and Z. Lai, *J. Am. Chem. Soc.*, **133**, 14896 (2011).
15. W. S. Wang, D. H. Wang, W. G. Qu, L. Q. Lu and A. W. Xu, *J. Phys. Chem. C*, **116**, 19893 (2012).
16. F. Zhao, B. Dong, R. Gao, G. Su, W. Liu and L. Shi, *Appl. Surf. Sci.*, **351**, 303 (2015).
17. D. S. Su, S. Perathoner and G. Centi, *Chem. Rev.*, **113**, 5782 (2013).
18. L. Lai, J. R. Potts, D. Zhan, L. Wang, C. K. Poh, C. Tang, H. Gong, Z. Shen, J. Y. Lin and R. S. Ruoff, *Energy Environ. Sci.*, **5**, 7936 (2012).
19. R. Asahi, T. Morikawa, T. Ohwaki, K. Aoki and Y. Taga, *Science*, **293**, 269 (2001).
20. Z. Jiang, F. Yang, N. J. Luo, T. Y. B. Chu, D. Sun, H. H. Shi, T. C. Xiao and P. E. Peter, *Chem. Commun.*, **47**, 6372 (2008).
21. W. Sang, C. Zhan, S. Hao, L. Mei, J. Cui, Q. Zhang, X. Jin and C. Li, *J. Wat. Pro. Eng.*, **41**, 101997 (2021).
22. L. Wen, T. Huang, M. Huang, Z. Lu, Q. Chen, Y. Meng and L. Zhou, *Ceram. Int.*, **46**, 9930 (2020).
23. K. Santhosh, S. K. Saddam, S. Chouti, S. Gonuguntla, S. P. Ega, A. Tiwari and U. Pal, *J. Mol. Structure*, **1235**, 130222 (2021).
24. P. Cheng, Z. Yang, H. Wang, W. Cheng, M. X. Chen, W. F. Shangguan and G. Ding, *Int. J. Hydrogen Energy*, **37**, 2224 (2012).
25. Y. Hu, M. Wang, F. Hu, J. Wu, L. Xu, G. Xu, Y. Jian and X. Peng, *Colloids Surf. A: Physicochem. Eng. Aspects*, **598**, 124831 (2020).
26. A. K. Geim, *Science*, **324**, 1530 (2009).
27. H. Fan, G. Yi, X. Zhang, B. Xing, C. Zhang, L. Chen and Y. Zhang, *Optical Mater.*, **111**, 110582 (2021).
28. J. Du, X. Lai, N. Yang, J. Zhai, D. Kisailus and F. Su, *ACS Nano*, **5**, 590 (2011).
29. C. Chen, W. M. Cai, M. Long, B. X. Zhou, Y. H. Wu and D. Y. Wu, *ACS Nano*, **4**, 6425 (2010).
30. H. V. Bao, N. M. Dat, N. T. H. Giang, D. B. Thinh, L. T. Tai, D. N. Trinh, N. D. Hai, N. A. D. Khoa, L. M. Huong, H. M. Nam, M. T. Phong and N. H. Hieu, *Surf. Interfaces*, **23**, 100950 (2021).
31. A. Zaleska, *Recent. Patents Eng.*, **2**, 157 (2008).
32. C. Berger, Z. Song, T. Li, X. Li, A. Y. Ogbazghi and R. Feng, *J. Phys. Chem. B.*, **108**, 19912 (2004).
33. M. Mohammadi, M. R. Roknabadi, M. Behdania and A. Kompany, *Ceram. Int.*, **45**, 12625 (2019).
34. F. Y. Pei, Y. L. Liu, S. G. Xu, J. Lu, C. X. Wang and S. K. Cao, *Int. J. Hydrogen Energy*, **38**, 2670 (2013).
35. S. Ida, P. Wilson, B. Neppolian, M. Sathish, P. Karthik and P. Ravi, *Ultrason. Sonochem.*, **57**, 62 (2019).
36. C. J. Brinker and G. W. Scherrer, *J. Non-Crystalline Solids.*, **70**, 301 (1985).
37. L. F. Lai, J. R. Potts, D. Zhan, L. Wang, C. KokPoh, C. Tang, H. Gong, Z. X. Shen, J. Linc and R. S. Ruoff, *Energy Environ. Sci.*, **5**, 7936 (2012).
38. Y. L. Liao, Y. Gao, S. M. Zhu, J. S. Zheng, Z. X. Chen, C. Yin, X. H. Lou and D. Zhang, *ACS Appl. Mater. Interfaces*, **7**, 35 (2015).
39. S. Stankovich, D. Dikin, R. D. Piner, K. Kohlhaas, A. Kleinhammes, Y. Jia, Y. Wu, S. T. Nguyen and R. S. Ruoff, *Carbon N. Y.*, **45**, 1558 (2007).
40. G. Wang, B. Wang, J. Park, J. Yang, X. Shen and J. Yao, *Carbon N. Y.*, **47**, 68 (2009).
41. X. Yin, H. Zhang, P. Xu, J. Han, J. Li and M. He, *RSC Adv.*, **3**, 18474 (2013).
42. D. Xu, P. Wang and B. Shen, *Digest J. Nanomat. Biostruct.*, **11**, 15 (2016).
43. Y. N. Hao, H. L. Guo, L. Tian and X. F. Kang, *RSC Adv.*, **5**, 43750 (2015).
44. N. Edwin, S. Saranya and P. Wilson, *Ceram. Int.*, **45**, 5475 (2019).
45. L. C. Chen, Y. C. Ho, W. S. Guo, C. M. Huang and T. C. Pan, *Electrochim. Acta.*, **54**, 3884 (2009).
46. O. Akhavan, M. Abdolahad, Y. Abdi and S. Mohajerzadeh, *Carbon*, **47**, 3280 (2009).
47. H. T. Yu, X. Quan, S. Chen, H. M. Zhao and Y. B. Zhang, *J. Photochem. Photobiol. A: Chem.*, **200**, 301 (2008).
48. O. Akhavan, R. Azimirad, S. Safa and M. M. Larijani, *J. Mater. Chem.*, **20**, 7386 (2010).

49. M. I. Carreño-Lizcano, A. F. Gualdrón-Reyes, V. Rodríguez-González, J. A. Pedraza-Avella and M. E. Niño-Gómez, *Cat. Today*, **341**, 96 (2020).
50. H. Zhang, X. J. Lv, Y. M. Li, Y. Wang and J. H. Li, *ACS Nano*, **4**, 380 (2010).
51. C. Wang, P. Zhou, Z. Wang, Y. Liu, P. Wang, X. Qin, X. Zhang, Y. Dai, M. H. Whangbo and B. Huang, *RSC Adv.*, **8**, 12841 (2018).
52. Y. Jin, C. Li and Y. Zhang, *New Carbon Mater.*, **35**, 394 (2020).
53. T. Song, L. Zhang, P. Y. Zhang, J. Zeng, T. T. Wang, A. Ali and H. P. Zeng, *J. Mater. Chem. A.*, **5**, 6013 (2017).
54. L. Q. Xu, L. Wang, B. Zhang, C. H. Lim, Y. Chen, K. G. Neoh, E. T. Kang and G. D. Fu, *Polymer*, **52**, 2376 (2011).
55. H. S. Yen, K. W. Yang, S. L. Tu and S. J. Chang, *Appl. Phys. Lett.*, **99**(1-3), 163102 (2011).
56. C. Lai, M.-M. Wang, G.-M. Zeng, Y.-G. Liu, D.-L. Huang, C. Zhang, R.-Z. Wang, P. Xu, M. Cheng, C. Huang, H. P. Wu and L. Qin, *Appl. Surf. Sci.*, **390**, 368 (2016).
57. D. Zhao, G. Sheng, C. Chen and X. Wang, *Appl. Catal. B Environ.*, **303**, 111 (2012).
58. M. Ceotto, L. L. Presti, G. Cappelletti, D. Meroni and F. Spadavecchia, R. Zecca, *Phys. Chem. C.*, **116**, 1764 (2012).
59. Y. N. Hao, H. L. Guo, L. Tian and X. F. Kang, *RSC Adv.*, **5**, 43750 (2015).
60. Y. J. Liu, J. X. Zhao and Q. H. Caiab, *Phys. Chem. Chem. Phys.*, **18**, 5491 (2016).